Nanotubular Geometry for Stabilizing Metastable 1T-Phase Ru Dichalcogenides

Myeong-Geun Kim, Seung-Hoon Kim, Jue-Hyuk Jang, Dong Wook Lee, Daeil Choi, Jae-Hyun Park, Kug-Seung Lee, Nanjun Chen, Chuan Hu, Young Moo Lee, and Sung Jong Yoo*

Owing to their remarkable electrochemical activities, 1T phase transition metal dichalcogenide (TMD) materials have attracted considerable interest in recent decades. However, metastable 1T phases are difficult to prepare and readily change phases. Therefore, for the first time, a monolayer nanotubular 1T Ru dichalcogenide comprising 92% of the 1T phase is synthesized, which is the highest value ever obtained using solvothermal methods. In the tubular geometry, the 1T phase exhibits superior durability against various external stimuli and electrocatalytic activity toward the oxygen reduction reaction. According to density-functional-theory-based and molecular dynamics calculations, sufficiently curved architectures can change their bond identities to safely maintain 1T phases, hence providing a strategy for stabilizing metastable phases. The study results form a basis for extensively applying 1T phases and will stimulate interest for applying tubular structures for stabilizing metastable materials.

1. Introduction

Polymorphism is a key transition metal dichalcogenide (TMD) feature, and various TMD polymorphic-phase-associated properties have recently emerged. For example, TMDs can exhibit transition-metal-coordination-based metallic 1T (or 1T′) [(distorted) octahedral] and semiconducting 2H (trigonal–prismatic) phases. Compared to the semiconducting (or insulating) phases, the metallic ones have exhibited notable activities in various electrochemical fields such as water splitting, supercapacitors, and lithium/sodium batteries.[1–5] Unfortunately, however, the metastable 1T phase requires a higher formation energy (ΔE_{form}) than the thermodynamically stable 2H phase. Hence, bottom-up methods for synthesizing TMDs usually produce 2H-dominated phases containing unsatisfactory 1T contents (e.g., 50–83%), and TMDs containing ≈100% of the 1T phase can only be synthesized using time-consuming processes [e.g., chemical vapor transport and chemical vapor deposition].[6–8]

Even if a high 1T phase content is obtained, the 1T phase reverts to the more thermodynamically stable 2H (or cubic) phase under ambient conditions.[7,9,10] To overcome this limitation, several strategies (such as alkali metal intercalation, plasma induction, and defect and strain engineering) for preparing high-purity and stabilized 1T-phase-containing materials have been reported. Ma et al. showed that the co-intercalation of alkali metal cations (Li+, Na+, and K+) can expand the interlayer spacing of MoS_2, thereby enhancing its phase stability.[11] Additionally, the presence of defects changed the electronic structure of pristine $PdSe_2$, which subsequently stabilized the metastable monoclinic polymorphic phase.[12] Very recently, Huang et al. demonstrated that monolayer 1T MoS_2 exhibits

---

M.-G. Kim, S.-H. Kim, J.-H. Jang, D. W. Lee, D. Choi, J.-H. Park, S. J. Yoo
Center for Hydrogen Fuel Cell Research
Korea Institute of Science and Technology
5 Hwarang-ro 14-gil, Seongbuk-gu, Seoul 02792, Republic of Korea
E-mail: ysj@kist.re.kr

The ORCID identification number(s) for the author(s) of this article can be found under https://doi.org/10.1002/aenm.202203133.

J.-H. Park, S. J. Yoo
Division of Energy & Environment Technology
KIST School
University of Science and Technology (UST)
Daejeon 34113, Republic of Korea

K.-S. Lee
Pohang Accelerator Laboratory (PAL)
Pohang University of Science and Technology (POSTECH)
Pohang 37673, Republic of Korea

N. Chen, C. Hu, Y. M. Lee
Department of Energy Engineering
College of Engineering
Hanyang University
Seoul 04763, Republic of Korea

S. J. Yoo
KHU–KIST Department of Converging Science and Technology
Kyung Hee University
Seoul 02447, Republic of Korea

excellent durability for the hydrogen evolution reaction in 0.5 M H_2SO_4 electrolyte.[13] The authors argued that although the insufficient strain is observed in the sheet-type 1T MoS_2, an appropriate amount of strain helps to modify the electronic structure and maintain the phase stability of the material.

In this study, we used a facile heat up method to prepare a rigatoni nanotube (RNT)-shaped 1T-phase-dominant Ru dichalcogenide. The RNTs were produced with various compositions, and a high 1T phase content of 92% was obtained at the optimal S/Se ratio. All the RNTs consisted of monolayer $Ru(S_xSe_{1-x})_{2-\delta}$ and exhibited an ultrasmall diameter (∅1.5 nm), short length ($d = 6.1$ nm), and high surface curvature. Interestingly, in the nanotubular structure, the 1T phase exhibited resistance against various external stimuli including electrochemical durability tests, long-term air exposure, and thermal annealing. Density-functional-theory-based/molecular dynamics (DFT/MD) calculations confirmed that the 1T-phase RNT structural stability was attributed to the strong coupling between the Ru and chalcogen atoms by an orbital overlap of ≈100%.[14] By extension, compared to previously reported TMD-based electrocatalysts,

the 1T-phase-dominant RNT effectively catalyzed oxygen reduction reaction (ORR) in both half- and full-cell ($E_{1/2} = 0.864$ eV and $W_{max} = 0.526$ W cm^{-2}, respectively) configurations.[15,16] While many studies have been focused on zero-dimensional and 2D-nanostructured electrocatalysts, our demonstration could be a crucial cornerstone of the importance of 1D nanotube structures.

2. Results

2.1. Synthesis and Characterization of $Ru(S_xSe_{1-x})_{2-\delta}$ RNTs

We used a seed-mediated growth mechanism to prepare single-walled $Ru(S_xSe_{1-x})_{2-\delta}$ RNTs. The experimental procedure is shown in **Figure 1**a. Briefly, a solution containing ruthenium acetylacetone [$Ru(acac)_3$], sulfur (S), selenium (Se), and carbon (C) powder was heated in oleylamine (OLA) and oleic acid (OA). The full details of the synthesis are provided in the Supporting Information. Initially, irregular Ru nanoparticles (NPs)
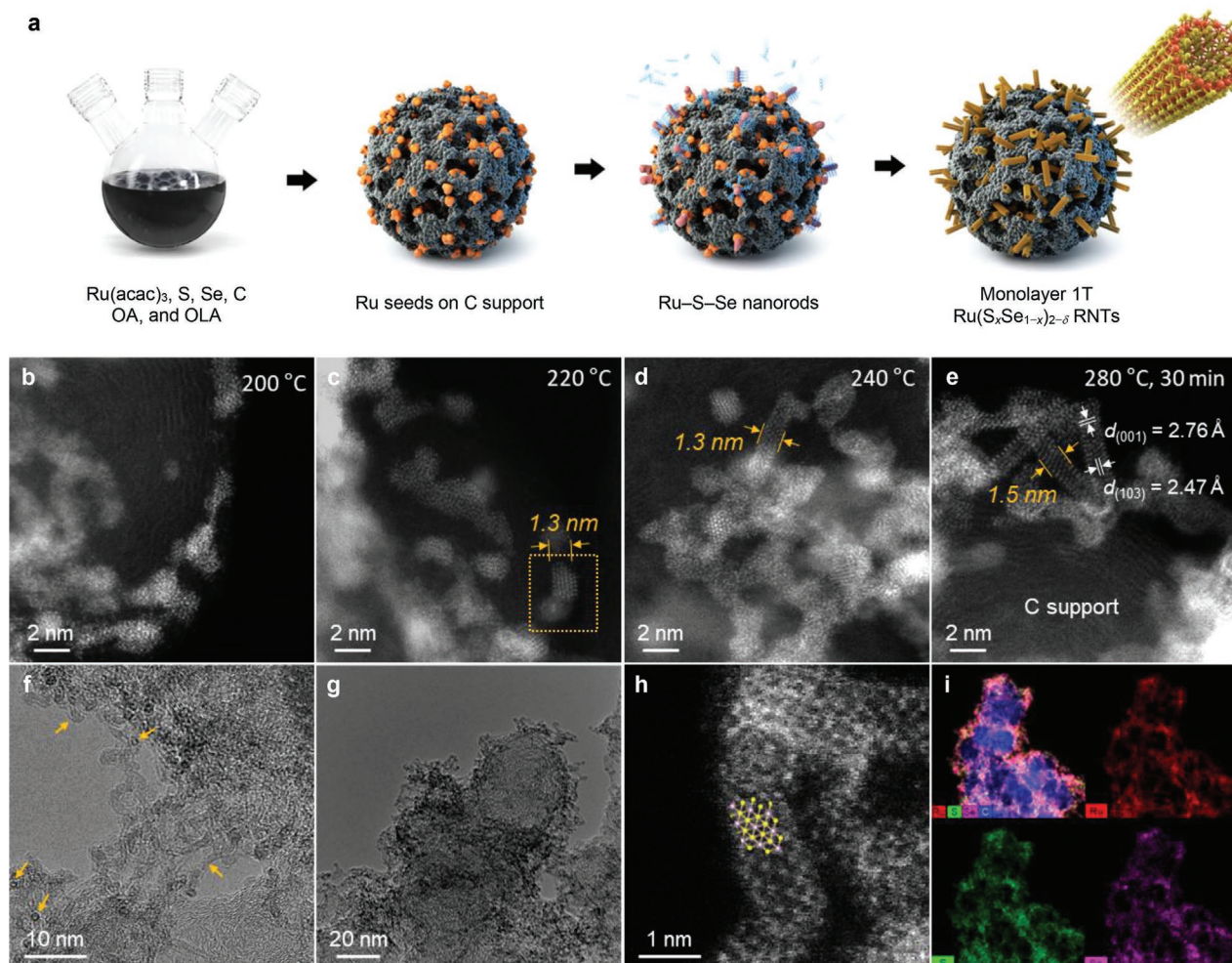
Figure 1. a) Schematic showing process for synthesizing $Ru(S_xSe_{1-x})_{2-\delta}$ RNTs by seed-mediated growth. Time-dependent STEM images collected during $Ru(S_{0.8}Se_{0.2})_{2-\delta}$ RNT b) seed formation, c,d) nanorod growth, and e) subsequent crystallization. f,g) TEM and h) high-resolution STEM images of product obtained at 280 °C for 30 min and corresponding 1T-armchair-structured atomic model. i) EDS elemental mapping images of $Ru(S_{0.8}Se_{0.2})_{2-\delta}$ RNTs dispersed on carbon supports. Ru, S, Se, and C atoms indicated by red, green, magenta, and blue, respectively.

**ADVANCED
SCIENCE NEWS**

www.advancedsciencenews.com

**ADVANCED
ENERGY
MATERIALS**

www.advenergymat.de

were generated by the $Ru(acac)_3$ thermally decomposing on the surface of Vulcan XC–72 carbon support. Subsequently, nanorods grew on the small Ru seed particles with the aid of the oleate ligands, which acted as structural directing agents.[17] Finally, the nanorods crystallized into monolayer RNTs and the Ru seed NPs disappeared as the reaction proceeded (Figure S1, Supporting Information). In Figure 1b–e, time–dependent transmission electron microscopy (TEM) images explicitly show the morphological evolution from irregularly shaped particles to the tubular architectures on the C supports. Clearly, the alloy nanorods (⌀1.3 nm) crystallized and grew into monolayer RNTs (⌀1.5 nm).[18,19] Under the same synthesis conditions, $Ru(S_xSe_{1-x})_{2-\delta}$ RNTs were prepared with various compositions ($x = 0$, 0.2, 0.5, 0.8, or 1) simply by adjusting the precursor concentration ratios (Figure S2a–e, Supporting Information). Directly preparing catalysts on C supports offers many practical advantages for potential large-scale applications. The catalyst is usually loaded on the supporting material for practical use, and is preferably simply prepared in a minimum synthesis step.[20,21] Interestingly, the $Ru(S_xSe_{1-x})_{2-\delta}$ RNTs could also be prepared without any C supports, suggesting that the interaction between the product and C support did not play a key role in forming the tubular structure (Figure S2f–i, Supporting Information). Rather, organic ligands selectively adsorbing on the specific nanostructure plane could have contributed to the $Ru(S_xSe_{1-x})_{2-\delta}$ RNT directional growth (Figures S3 and S4, Supporting Information).[22] Especially, it is suggested that the combination of fatty acids and fatty amines is the suitable condition for the formation of nanotube structures (Figure S5, Supporting Information). All the characterization and electrochemical measurements were conducted using carbon-supported samples.

The high-resolution transmission electron microscopy (HRTEM) and scanning transmission electron microscopy (STEM) images indicate that $Ru(S_{0.8}Se_{0.2})_{2-\delta}$ exhibited a hexagonal 1T structure and a tubular architecture. The prepared RNTs exhibited lattice fringes of 2.47 and 2.76 Å, corresponding to the hexagonal (103) and (001) planes, respectively (Figure 1e).[1,23] The hollow interior of RNT confirmed the tubular structure (Figure 1f–g). Furthermore, the $Ru(S_{0.8}Se_{0.2})_{2-\delta}$ atomic structure corresponded to the crystal structural model comprising hexagonal 1T-phase armchair configurations (Figure 1h). Additionally, energy dispersive X-ray spectroscopy (EDS) elemental mappings confirmed that atomically well-mixed $Ru(S_xSe_{1-x})_{2-\delta}$ RNTs had formed on the C supports (Figure 1i). According to EDS maps, the $Ru(S_xSe_{1-x})_{2-\delta}$ RNTs exhibited an (S+Se)/Ru ratio < 2, indicating anion vacancies. Electron paramagnetic resonance (EPR) spectra were generated, and an anion vacancy-charge-state-related signal ($g = 2.003$) was clearly detected (Figure S6, Supporting Information).[24] The anion defects could be due to the atomically curved tubular structure.[25] Therefore, we denoted the anion-deficient RNTs as "$RuSe_{2-\delta}$," "$Ru(S_{0.2}Se_{0.8})_{2-\delta}$" "$Ru(S_{0.5}Se_{0.5})_{2-\delta}$," "$Ru(S_{0.8}Se_{0.2})_{2-\delta}$" and "$RuS_{2-\delta}$."

The high-resolution powder diffraction (HRPD) patterns and X-ray absorption spectroscopy (XAS) spectra consistently showed that Ru, S, and Se were atomically well-mixed in the RNT structure. As presented in **Figure 2**a, all the samples exhibited HRPD patterns consistent with hexagonally

structured TMDs. Although very few reports on hexagonal RuX_2 RuX_2 (X = S, Se or Te) are available in the literature, the $Ru(S_xSe_{1-x})_{2-\delta}$ HRPD patterns are clearly different from those of cubic RuX_2, Ru, or RuO_2. According to Bragg's law, the minimum $Ru(S_xSe_{1-x})_{2-\delta}$ interlayer spacing was calculated as ≈0.8 nm, indicating that the ⌀1.5-nm $Ru(S_xSe_{1-x})_{2-\delta}$ RNT comprised a monolayer sheet.[26] Moreover, the $Ru(S_xSe_{1-x})_{2-\delta}$ RNTs were measured using XAS to investigate the local crystal structures. The X-ray absorption near-edge structure (XANES) spectra are presented in Figure 2b wherein a composition-dependent peak shift appeared in the Ru K-rising edge region,[25] which could be attributed to the charge transfer from Ru to chalcogen atoms because their electronegativities are different (i.e., Ru, S, and Se = 2.2, 2.58, and 2.55, respectively). Figure 2c presents the Fourier-transform (FT) spectra in the R space for the k^2-weighted extended X-ray absorption fine-structure (EXAFS) spectra generated for the $Ru(S_xSe_{1-x})_{2-\delta}$ RNTs. The spectra for all the $Ru(S_xSe_{1-x})_{2-\delta}$ RNTs exhibited a distinct peak between Ru−Se and Ru−S bonds (2.06 and 1.81 Å, respectively), suggesting that most Ru atoms were coordinated with chalcogen ones. Increasing the Se content expanded the interatomic distance because Se atoms are larger than S ones. However, because the average interatomic distance is measured along all the crystallographic directions, the tubular structure exhibited broad Ru–X (X = S or Se) peaks under both tensile and compressive strains.[27] Meanwhile, the RNT Ru−Ru bond (2.53 Å) could originate from unsaturated Ru atoms.[28,29]

The X-ray photoelectron spectroscopy (XPS) spectra clearly revealed that the $Ru(S_xSe_{1-x})_{2-\delta}$ RNTs mainly comprised the 1T phase. XPS is regarded as the most reliable technique that can be used to quantitatively measure 1T-phase-containing materials.[3,4,30] The XPS Ru 3d, S 2p, Se 3d, and valence band spectra are presented to investigate the elemental composition and chemical states. Additionally, because the Ru $3d_{3/2}$ and C 1s peaks are almost superposed, Ru $3d_{5/2}$ spectrum is presented (Figure 2d). With increasing S content, Ru 3d binding energy positively shifted because Ru and S exhibit different electronegativities. However, the S-rich sample [$Ru(S_{0.8}Se_{0.2})_{2-\delta}$] did not exhibit a linear relationship between the composition and binding energy, suggesting that the S-rich sample contained a particularly high 1T-to-2H-phase ratio. Compared to the 2H-phase binding energy, the 1T phase one is typically shifted by ≈−0.8 eV because the 1T phase exhibits a partially unfilled orbital.[3,31] The S 2p and Se 3d XPS spectra clearly exhibited a similar trend (Figure 2e,f, respectively). The 1T phase content was quantitatively analyzed using the Se 3d peak because other peaks did not interfere with it. The ratio of Se-free $RuS_{2-\delta}$ was obtained using the S 2p spectrum, confirming that all the samples contained a dominant 1T phase. The 1T phase contents were ranked in descending order as follows: $Ru(S_{0.8}Se_{0.2})_{2-\delta}$ > $RuSe_{2-\delta}$ > $Ru(S_{0.2}Se_{0.8})_{2-\delta}$ > $Ru(S_{0.5}Se_{0.5})_{2-\delta}$ > $RuS_{2-\delta}$, which contained 92%, 89%, 75%, 74%, and 62% of the 1T phase, respectively, and is consistent with the 1T phase contents obtained using the Ru $3d_{5/2}$ peak (Table S1, Supporting Information). Furthermore, for a clear comparison, XPS analysis of the 2H Ru dichalcogenides (i.e., RuS_2 and $RuSe_2$) synthesized according to the previously reported method was conducted (Figure S7, Supporting Information).[2] Additionally, the position of d-band center (ε_d) is plotted as a function of the 1T phase content
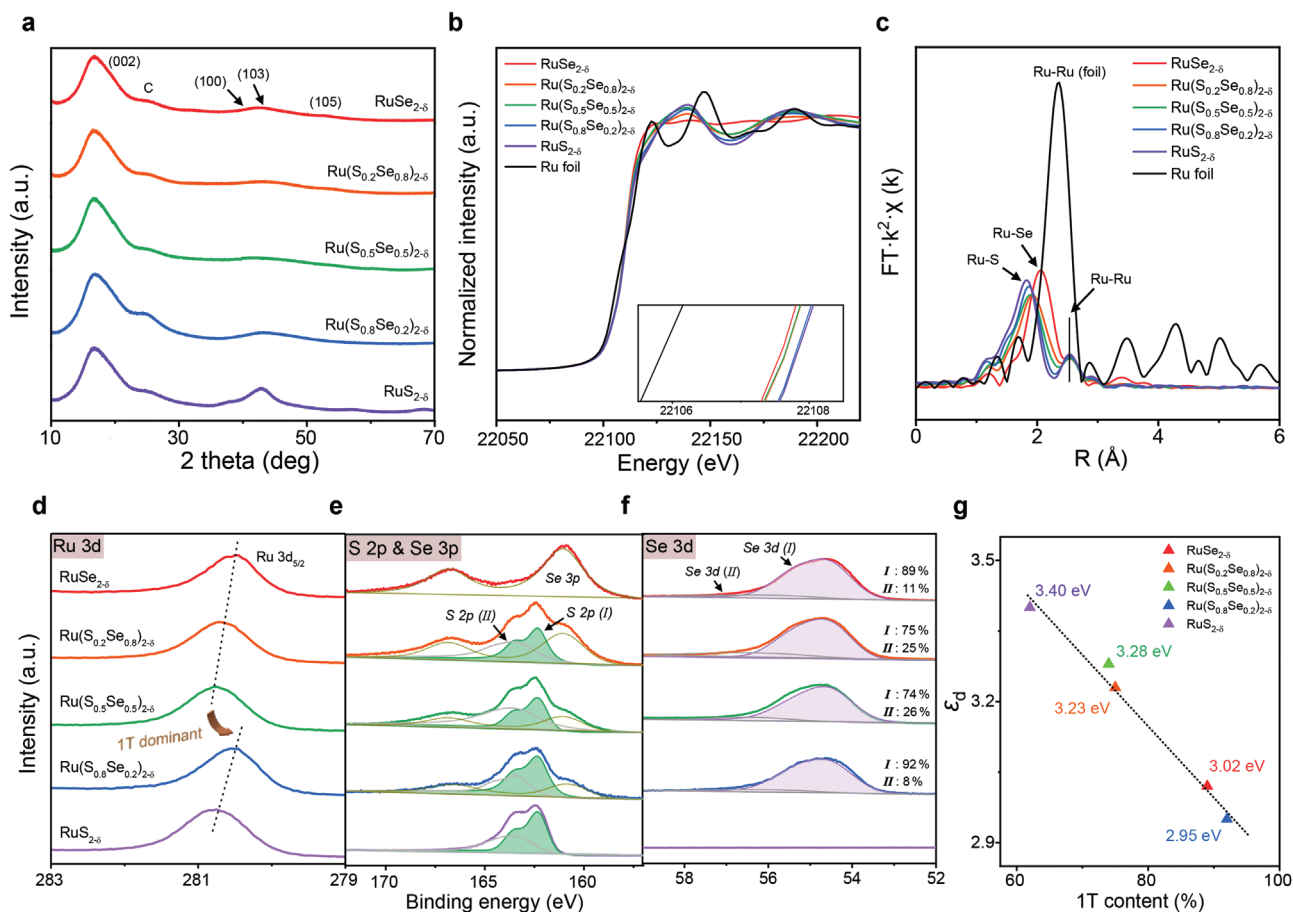
Figure 2. $Ru(S_xSe_{1-x})_{2-\delta}$ RNT (x = 0, 0.2, 0.5, 0.8, or 1) structural and chemical composition analyses: a) HRPD patterns and b) XANES and c) EXAFS spectra. d) Ru $3d$, (e) S $2p$ and Se $3p$, and f) Se $3d$ XPS spectra. Dotted lines in (d) indicate that S-rich sample exhibited different peak shifts. Deconvoluted spectra for chalcogen atoms correspond to 1T and 2H phases (I and II, respectively). g) Valence-band-calculated d-band central position plotted as function of 1T-phase content.

(Figure 2g). Usually, 1T-phase-related ε_d values are lower than 2H ones. The ε_d values are ranked in ascending order as follows: $Ru(S_{0.8}Se_{0.2})_{2-\delta}$ < $RuSe_{2-\delta}$ < $Ru(S_{0.2}Se_{0.8})_{2-\delta}$ < $Ru(S_{0.5}Se_{0.5})_{2-\delta}$ < $RuS_{2-\delta}$, which correspond to binding energies of 2.95, 3.02, 3.23, 3.28, and 3.40 eV.[1] The strong correlation between ε_d and the 1T phase content suggested that the latter was one of the main electrocatalytic activity determiners. Additionally, the Fermi-edge cutoff indicated that all the samples, even the monolayer ones, exhibited metallic characteristics (Figure S8, Supporting Information). The mass of Ru supported on each sample is shown in Table S2 (Supporting Information).

2.2. $Ru(S_xSe_{1-x})_{2-\delta}$ RNT Structural Stability Investigated Using First-Principles Calculations

Density functional theory (DFT)-based first-principles computations revealed the tubular RNT atomic arrangements and electronic structures wherein the 1T phase was stable. Metastable 1T phases usually suffer from unwanted phase transitions and unsatisfactory phase purities. Owing to their high surface energies, even 2D-layered 1T TMDs restack.[32] Likewise, bulk 1T- Ru dichalcogenides (i.e., RuS_2, $RuSe_2$, and $RuS_{1.5}Se_{0.5}$)

are less stable than their 2H counterparts, (A in **Figure 3**a). Unlike binary systems, however, the ternary systems tends to exist in a monolayer than a stacked form (B in Figure 3a). In order to reveal the most stable morphology, the nanotube and nanosheet ΔE_{form} values were compared (C in Figure 3a). The RuS_2 and $RuSe_2$ nanotubes were stable regardless of their diameter. Meanwhile, the ternary sample was a monolayer when the diameter was >2 nm and a nanotube only when the diameter was 1.5 nm (C_2 and C_3 in Figure 3a). That is, the 1T-phase nanotubes were stable when the diameter was as small as 1.5 nm regardless of their composition (C_1 in Figure 3a). The C_1 model exhibiting a diameter like that of the RNTs exhibited different bond identities (e.g., bond angles and lengths) originating from the bulk 1T-phase layer. The 1T phase fragments were linked by so-called "shared sulfides" to form a tubular structure.[33–35] Additionally, as previously reported, the larger and smaller Se and S atoms were on the nanotube exterior and interior, respectively, which markedly relaxed the strain (Figure S9, Supporting Information).[36] Moreover, the electronic structure of each nanotube was calculated to elucidate why the small-diameter nanotube exhibited improved structural durability. Figure 3b presents the densities of states (DOSs) of the Ru d and S and Se p orbitals in the $Ru(S_xSe_{1-x})_{2-\delta}$ RNTs exhibiting diameters C_1,
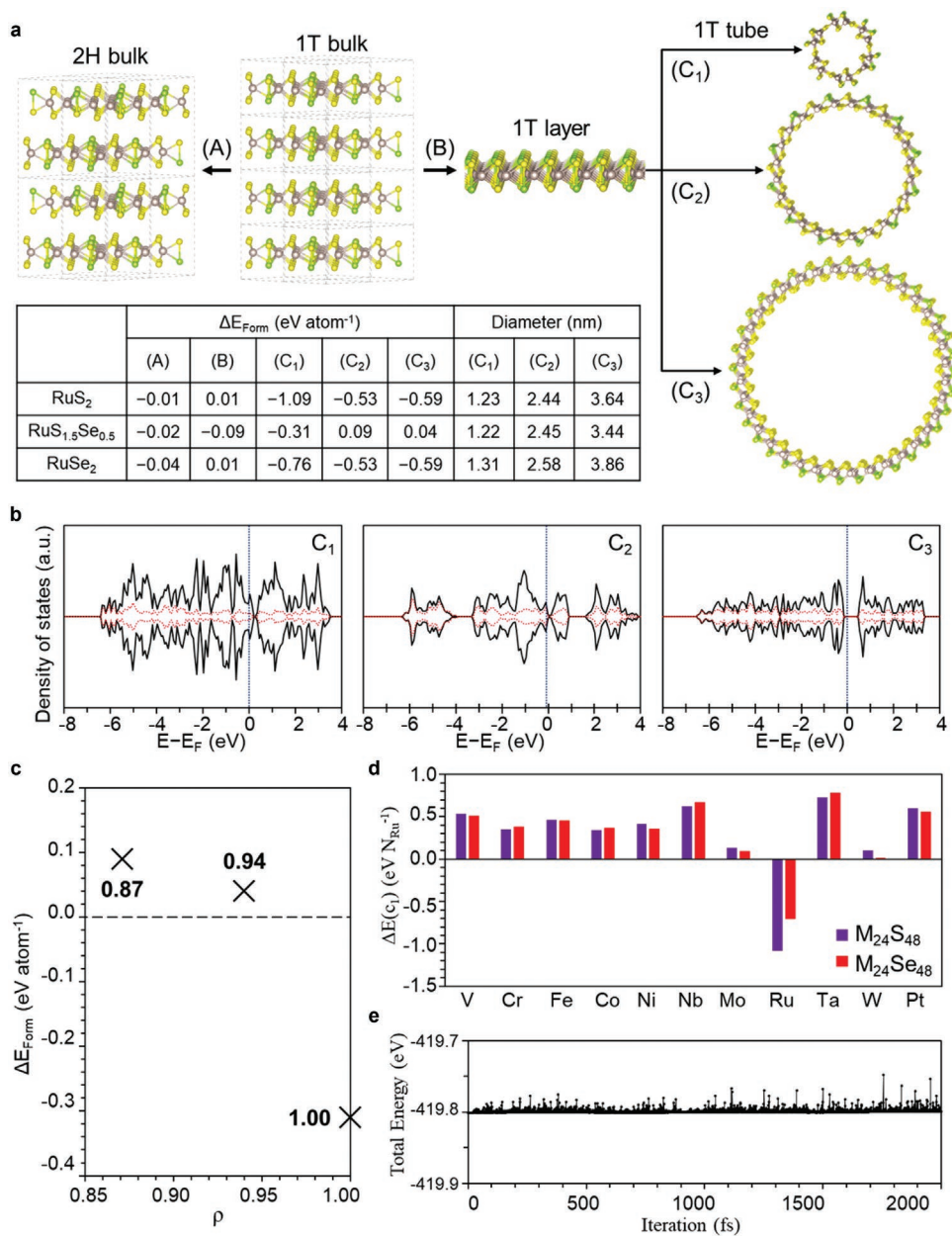
Figure 3. a) Formation energies (ΔE_{form}) of 2H and 1T bulks, 1T layer, and 1T nanotube exhibiting different diameters: $Ru_{24}(S_xSe_{1-x})_{48}$ (C_1), $Ru_{48}(S_xSe_{1-x})_{96}$ (C_2), and $Ru_{72}(S_xSe_{1-x})_{144}$ (C_3). b) Corresponding DOS for $Ru(S_xSe_{1-x})_2$ nanotube. Black solid and red and navy dotted lines represent Ru 4d orbital, S 3p and Se 4p orbitals, and Fermi energy level, respectively. c) Correlation between degree of p–d orbital overlap (ρ) and ΔE_{form}. d) Tube formation energies of previously reported $M_{24}X_{48}$-based 1T materials. e) Ab initio MD calculations for $Ru_{24}(S_xSe_{1-x})_{48}$ under NVT ensemble conditions at 250 °C.

C_2, and C_3 of 1.22, 2.45, and 3.44 nm, respectively. The interatomic mixing degree (ρ) was calculated from the fraction of p–d orbital overlap among the total S and Se atomic p orbitals. The results suggested that the smaller the RNT diameter, the more Ru atom d (i.e., Ru 4d) and chalcogen atom p (i.e., S 3p and Se 4p) orbitals overlapped.[37–39] Interestingly, when the diameter was 1.5 nm, the orbitals overlapped almost 100%, indicating the strong spin–orbit interaction between the Ru and chalcogen atoms (Figure 3c).[40,41] In other words, the introduction of sufficient surface curvature can modify the electronic structures and bond identities.[42,43] Additionally, the calculated DOSs showed

that the small-diameter nanotube (C_1) exhibited metallic behavior regardless of the composition, which is consistent with the XPS results (Figure S10, Supporting Information).

Furthermore, except for Ru, other 1T-phase-containing TMDs (MX_2, where M = V, Cr, Fe, Co, Ni, Nb, Mo, Ta, W, or Pt and X = S or Se) favorably exist as nanosheets rather than nanotubes (Figure 3d). Molybdenum (Mo) and tungsten (W) TMDs exhibit small albeit positive ΔE_{form} value, which could be because their d orbitals (i.e., Mo 4d and W 5d) are relatively adjacent to the chalcogen atom p orbitals,[44] suggesting that the orbital overlap degree is strongly related to
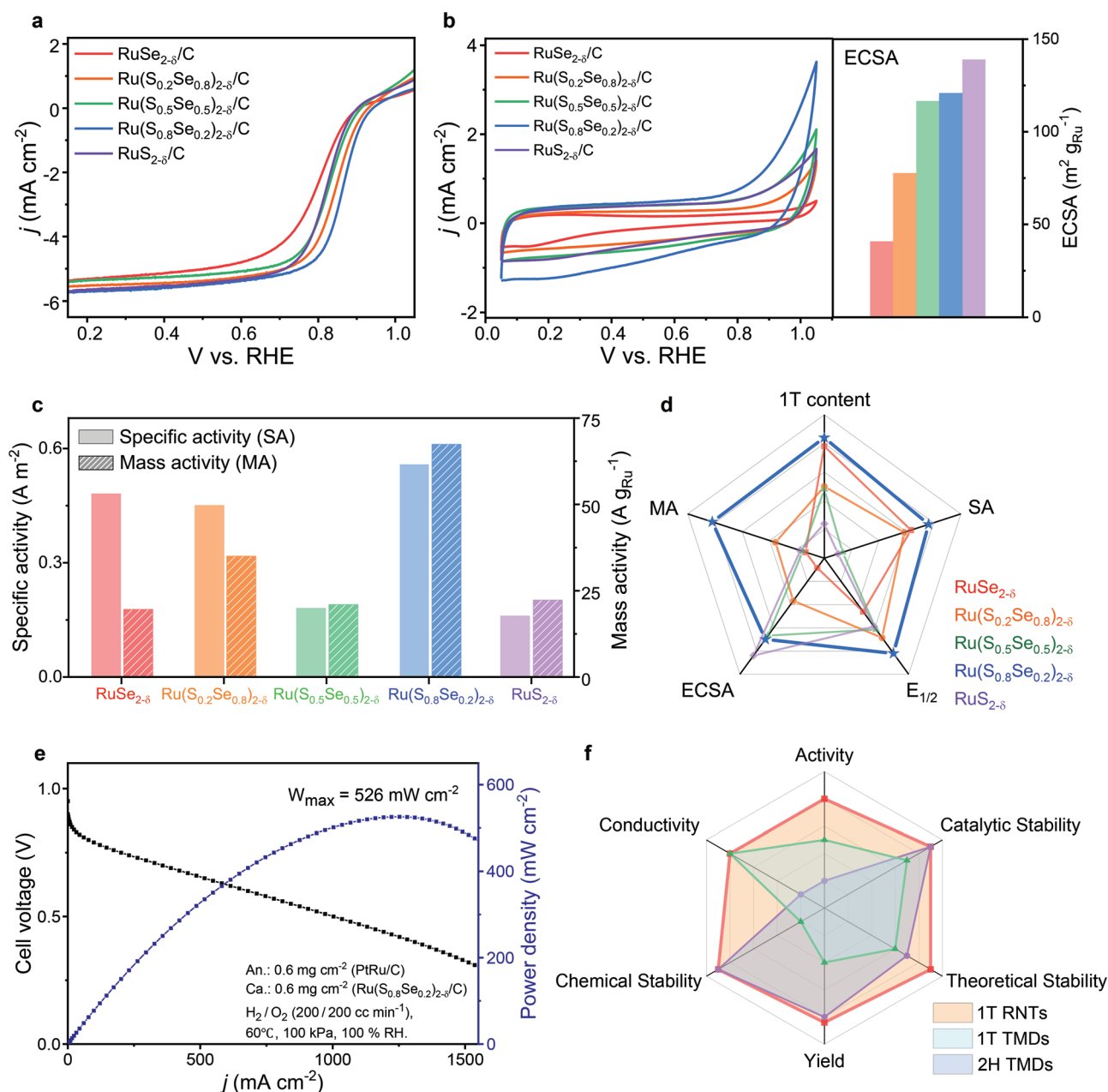
Figure 4. Electrocatalytic performances of $Ru(S_xSe_{1-x})_{2-\delta}$ RNTs in 0.1 M KOH: a) ORR LSV, and b) CV curves with corresponding ECSAs. c) SAs and MAs calculated at 0.85 V versus RHE. d) Radar chart comparing ORR activities of $Ru(S_xSe_{1-x})_{2-\delta}$ RNTs prepared with different 1T phase contents. H_2–O_2 single cell performances of $Ru(S_{0.8}Se_{0.2})_{2-\delta}$ RNTs: e) I–V polarization and power density curves. f) Performance score spider chart comparing catalytic activities, catalytic stabilities, theoretical stabilities, product yields, chemical stabilities, and electrical conductivities of 1T-RNT-, 1T-TMD-, and 2H-TMD-based electrocatalysts.

the nanotube structural stability. Because the stabilized Ru chalcogenide RNTs endured external stresses such as thermal shocks and electrochemical conditions, MD simulation was conducted at 250°C, and the total energy change was negligible (Figure 3e). The in situ X-ray diffraction (XRD) patterns consistently showed that crystal structure of $Ru(S_{0.8}Se_{0.2})_{2-\delta}$ RNT endured heating up to 300 °C and did not exhibit any observable changes in morphology, composition, or 1T phase content after heating (Figures S11 and S12, Supporting

Information). A peak corresponding to Ru metal was detected only when it was heated at 400 °C or more. After the ORR simulations, the ternary sample exhibited catalytic stability superior to those of the binary samples, while the Ru–S–Se RNTs exhibited negligible catalytic stability changes. Moreover, the binary sample structures changed and were partially distorted, S–S bonds were generated in RuS_2, and the $RuSe_2$ nanotubes were slightly distorted (Figure S13, Supporting Information).

**ADVANCED
SCIENCE NEWS**

www.advancedsciencenews.com

**ADVANCED
ENERGY
MATERIALS**

www.advenergymat.de

2.3. Electrocatalytic Activities in Alkaline Electrolytes

The electrocatalytic activities of the $Ru(S_xSe_{1-x})_{2-\delta}$ RNTs toward ORRs were evaluated using 0.1 M KOH electrolyte. As presented in **Figure 4**a, the 1T-phase-dominant $Ru(S_{0.8}Se_{0.2})_{2-\delta}$ RNT half-wave potential ($E_{1/2}$ = 0.864 eV), which is comparable to those of commercial Pt/C catalysts, outperformed those of the other samples. The electrochemically active surface area (ECSA) was determined using cyclic voltammetry (CV) measurements. The ECSA increased with increasing S content (Figure 4b). Usually, catalysts are compared by comparing their specific activities (SAs) and mass activities (MAs) (Figure 4c). The S-rich sample exhibited the highest SA and MA (0.5584 A m^{-2} and 67.4 A g$_{Ru}^{-1}$, respectively). Although catalytic activity depends on various material characteristics such as the ECSA, number of active sites, and electrical conductivity, the SAs (which indicate the intrinsic electrocatalyst activity) followed the same descending 1T-to-2H phase-ratio order as follows: $Ru(S_{0.8}Se_{0.2})_{2-\delta}$ > $RuSe_{2-\delta}$ > $Ru(S_{0.2}Se_{0.8})_{2-\delta}$ > $Ru(S_{0.5}Se_{0.5})_{2-\delta}$ > $RuS_{2-\delta}$, suggesting that in alkaline electrolytes, the ORR activities were strongly related to the 1T phase content.[43] As shown in Figure 4d, a radar chart compares the MA, ECSA,

$E_{1/2}$, and SA indicators of the $Ru(S_xSe_{1-x})_{2-\delta}$ RNT ORR activities. Additionally, the RNT catalytic activity was superior to that of its 2D layered counterpart, suggesting that the curved surface enhanced both the catalytic activity and structural stability (Figures S4 and S14, Supporting Information).[45] The ORR activity of carbon-free samples was also evaluated, and the tendency to be the same as that of carbon-supported samples in terms of $E_{1/2}$ (Figure S15, Supporting Information).

Moreover, the $Ru(S_{0.8}Se_{0.2})_{2-\delta}$ RNTs were applied as cathode materials in single-cell devices and exhibited a promising maximum power density (W_{max}) of 0.526 W cm^{-2}. Despite considerable research interest in 1T-phase TMD electrocatalysts, most studies to date have only focused on evaluating the electrochemical performance of these materials in half cells, which could be because 1T-phase TMD electrocatalysts exhibit low catalytic and chemical stabilities. Moreover, only a few studies on TMDs for application to alkaline fuel cells are available in the literature.[15,22] In this study, a membrane electrode assembly (MEA) was fabricated using of $Ru(S_{0.8}Se_{0.2})_{2-\delta}$ and PtRu/C as a cathode and an anode, respectively, to evaluate the electrochemical performance of the RNTs in a full cell. The mass loadings of both electrodes were 0.6 mg cm^{-2}. The polarization
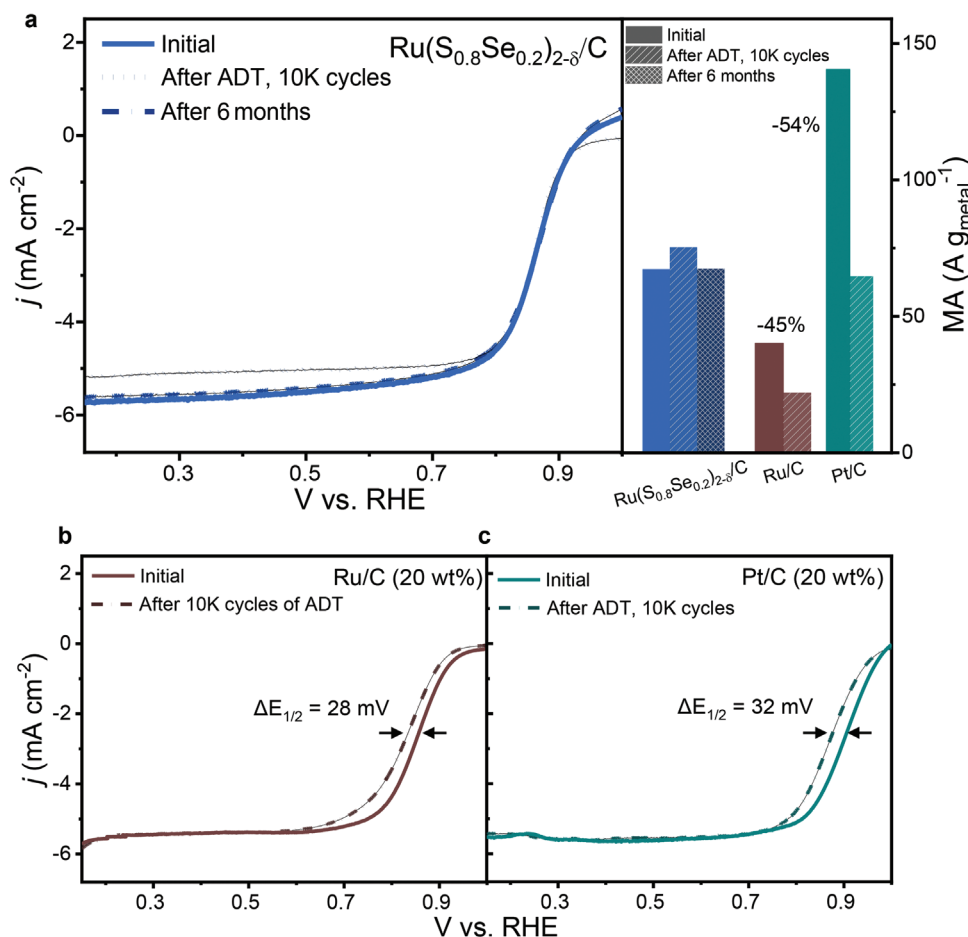
Figure 5. Electrocatalytic stabilities of $Ru(S_xSe_{1-x})_{2-\delta}$ RNTs: a) LSV curves generated before and after $Ru(S_{0.8}Se_{0.2})_{2-\delta}$ RNT ADT cycling or air exposure. Bar graphs show MA change after each test. ADTs were conducted by cycling $Ru(S_{0.8}Se_{0.2})_{2-\delta}$ RNTs 10000 times between 0.6 and 1.0 V versus RHE at 100 mV s^{-1}. Air-exposed sample was stored under ambient conditions in laboratory for 6 months. For references, LSV curves were generated before and after ADT cycling for commercial 20 wt% b) Ru/C and c) Pt/C.

2203133 (7 of 9)

curves generated for the $Ru(S_{0.8}Se_{0.2})_{2-\delta}$ clearly indicated that in a full-cell configuration, the tubular 1T-phase-containing RNTs exhibited electrocatalytic activities (Figure 4e) superior to those previously reported for TMD electrocatalysts in H_2–O_2 anion exchange membrane fuel cells (AEMFCs) (Table S3, Supporting Information). To optimize the RNT ionomer content and show that the 1T-phase RNTs could overcome the low stability of conventional 1T-phase TMD materials, I–V curves were generated for the RNTs prepared using various ionomer contents (Figure S16, Supporting Information). As shown in Figure 4f, the catalytic activities, stabilities, product yields, and conductivities were compared for 1T-phase RNTs and conventional 1T- and 2H-phase TMD materials.[46] Group 4 and 5 TMDs are easily oxidized in ambient air or reaction solutions within minutes to hours.[8,10,46] Additionally, 1T-phase TMDs are usually formed as intermediate phases, leading to poor phase purities and product yields.[47] However, the experimental measurements and theoretical calculations in this study showed that the 1T-phase RNTs exhibited superior structural stabilities without sacrificing the catalytic activities.

Furthermore, the $Ru(S_{0.8}Se_{0.2})_{2-\delta}$ RNT electrochemical durabilities were confirmed using standard accelerated durability tests (ADTs). As presented in **Figure 5**a, the ORR activities remained stable after 10k ADT cycles. Moreover, the morphology and composition negligibly changed (Figure S17, Supporting Information). In contrast, commercial 20 wt% Ru/C and Pt/C catalysts (Premetek) both noticeably degraded during ADT cycling, exhibiting half-wave potential ($\Delta E_{1/2}$) decreases of 28 and 32 mV, respectively (Figure 5b,c). After 10k ADT cycles, the Ru/C and Pt/C MAs decreased 45% and 54%, respectively (Figure 5a bar graphs). Because the electrode surfaces oxidized during ADT cycling, MA was used instead of SA as a comparative index (Figure S18, Supporting Information). Moreover, the $Ru(S_{0.8}Se_{0.2})_{2-\delta}$ RNTs exhibited superior stability in air. Although 1T-phase TMDs revert to the stable 2H phase under ambient conditions, the ORR performances as well as 1T phase ratio of RNT were maintained even after the 1T-phase TMDs was exposed to ambient air at room temperature for 6 months (Figure S19, Supporting Information).[7,8,10,48]

3. Conclusions

Despite 1T-phase TMDs exhibiting diverse application potential, their poor stability and low phase purity have hindered their further development. Hence, developing a method for synthesizing stabilized 1T-phase-dominant materials is very desirable. The results of this study suggest that a tubular geometry can stabilize the unique 1T phase in TMDs and enable 1T-phase TMDs to be utilized in many applications. Owing to ≈100% orbital overlap, the strong bonding between the Ru and chalcogen atoms in the tubular structure stabilized the 1T phase. The 1T-phase RNTs were structurally stable under various conditions (e.g., during the electrochemical, oxidation, thermal durability tests). Moreover, owing to their high 1T-to-2H-phase ratio (92%), the $Ru(S_xSe_{1-x})_{2-\delta}$ RNTs exhibited superior ORR catalytic activities ($E_{1/2}$ = 0.864 eV, and W_{max} = 0.526 W cm^{-2}) compared to those of conventional TMDs, which highlights the importance of stabilizing tubular 1T-phase TMDs for boosting electrocatalytic activity.

Supporting Information

Supporting Information is available from the Wiley Online Library or from the author.

Conflict of Interest

The authors declare no conflict of interest.

Data Availability Statement

The data that support the findings of this study are available from the corresponding author upon reasonable request.

[1] C. Zhu, D. Gao, J. Ding, D. Chao, J. Wang, *Chem. Soc. Rev.* **2018**, *47*, 4332.

[2] Y. Zhao, H. Cong, P. Li, D. Wu, S. Chen, W. Luo, *Angew. Chem.* **2021**, *133*, 7089.

[3] Y. Li, Y. Zhang, X. Tong, X. Wang, L. Zhang, X. Xia, J. Tu, *J. Mater. Chem. A* **2021**, *9*, 1418.

[4] Y. Chen, Z. Lai, X. Zhang, Z. Fan, Q. He, C. Tan, H. Zhang, *Nat. Rev. Chem.* **2020**, *4*, 243.

[5] Z. Lai, Q. He, T. H. Tran, D. V. M. Repaka, D. D. Zhou, Y. Sun, S. Xi, Y. Li, A. Chaturvedi, C. Tan, B. Chen, G. H. Nam, B. Li, C. Ling, W. Zhai, Z. Shi, D. Hu, V. Sharma, Z. Hu, Y. Chen, Z. Zhang, Y. Yu, X. Renshaw Wang, R. V. Ramanujan, Y. Ma, K. Hippalgaonkar, H. Zhang, *Nat. Mater.* **2021**, *20*, 1113.

[6] X. Chen, Z. Wang, Y. Wei, X. Zhang, Q. Zhang, L. Gu, L. Zhang, N. Yang, R. Yu, *Angew. Chem., Int. Ed.* **2019**, *58*, 17621.

[7] C. Mattevi, M. S. Sokolikova, *Chem. Soc. Rev.* **2020**, *49*, 3952.

[8] Q. Fu, J. Han, X. Wang, P. Xu, T. Yao, J. Zhong, W. Zhong, S. Liu, T. Gao, Z. Zhang, L. Xu, B. Song, *Adv. Mater.* **2021**, *33*, 1907818.

[9] J. Peng, Y. Liu, X. Luo, J. Wu, Y. Lin, Y. Guo, J. Zhao, X. Wu, C. Wu, Y. Xie, *Adv. Mater.* **2019**, *31*, 1900568.

[10] Y. Yu, G. H. Nam, Q. He, X. J. Wu, K. Zhang, Z. Yang, J. Chen, Q. Ma, M. Zhao, Z. Liu, F. R. Ran, X. Wang, H. Li, X. Huang, B. Li, Q. Xiong, Q. Zhang, Z. Liu, L. Gu, Y. Du, W. Huang, H. Zhang, *Nat. Chem.* **2018**, *10*, 638.

[11] F. Liu, Y. Zou, X. Tang, L. Mao, L. Du, H. Wang, M. Zhang, Z. Wang, N. Yao, W. Zhao, M. Bai, T. Zhao, Y. Liu, Y. Ma, F. Liu, X. Tang, H. Wang, M. Zhang, Z. Wang, N. Yao, W. Zhao, M. Bai, T. Zhao, Y. Liu, Y. Ma, Y. Zou, L. Mao, D. Du, *Adv. Funct. Mater.* **2022**, *32*, 2204601.

[12] Y. Gu, L. Zhang, H. Cai, L. Liang, C. Liu, A. Ho, Y. Yu, A. Houston, A. A. Puretzky, G. Duscher, P. D. Rack, C. M. Rouleau, X. Meng, M. Yoon, D. B. Geohegan, K. Xiao, *ACS Nano* **2022**, *16*, 13900.

[13] Z. Liu, K. Nie, X. Qu, X. Li, B. Li, Y. Yuan, S. Chong, P. Liu, Y. Li, Z. Yin, W. Huang, *J. Am. Chem. Soc.* **2022**, *144*, 4863.

[14] K. Maiti, S. Maiti, M. T. Curnan, H. J. Kim, J. W. Han, *Adv. Energy Mater.* **2021**, *11*, 2101670.

[15] S. Sarkar, S. Patel, S. Sampath, *J. Power Sources* **2020**, *445*, 227280.

[16] H. P. Jhong, S. T. Chang, H. C. Huang, K. C. Wang, J. F. Lee, M. Yasuzawa, C. H. Wang, *Catal. Sci. Technol.* **2019**, *9*, 3426.

[17] K. Wang, B. Li, W. Wei, J. Wang, Q. Shen, P. Qu, *Nanoscale* **2020**, *12*, 23740.

[18] R. K. Ramamoorthy, A. Viola, B. Grindi, J. Peron, C. Gatel, M. Hytch, R. Arenal, L. Sicard, M. Giraud, J. Y. Piquemal, G. Viau, *Nano Lett.* **2019**, *19*, 9160.

[19] S. Liu, G. Chen, P. N. Prasad, M. T. Swihart, *Chem. Mater.* **2011**, *23*, 4098.

[20] J. Shim, J. Lee, Y. Ye, J. Hwang, S.-K. Kim, T.-H. Lim, U. Wiesner, J. Lee, *ACS Nano* **2012**, *6*, 6870.

[21] Z. Liu, Z. Zhao, Y. Wang, S. Dou, D. Yan, D. Liu, Z. Xia, S. Wang, *Adv. Mater.* **2017**, *29*, 1606207.

[22] Z. Wu, S. Yang, W. Wu, *Nanoscale* **2016**, *8*, 1237.

[23] H. He, D. Huang, Q. Gan, J. Hao, S. Liu, Z. Wu, W. K. Pang, B. Johannessen, Y. Tang, J. L. Luo, H. Wang, Z. Guo, *ACS Nano* **2019**, *13*, 11843.

[24] Y. Li, J. Li, J. Chen, P. Cai, G. Wang, Y. Hou, L. Lei, Z. Wen, *J. Power Sources* **2020**, *472*, 228625.

[25] K. Jiang, M. Luo, Z. Liu, M. Peng, D. Chen, Y. R. Lu, T. S. Chan, F. M. F. de Groot, Y. Tan, *Nat. Commun.* **2021**, *12*, 1687.

[26] W. S. V. Lee, T. Xiong, X. Wang, J. Xue, *Small Methods* **2021**, *5*, 2000815.

[27] J. S. Kim, H. K. Kim, S. H. Kim, I. Kim, T. Yu, G. H. Han, K. Y. Lee, J. C. Lee, J. P. Ahn, *ACS Nano* **2019**, *13*, 4761.

[28] Z. Luo, Y. Ouyang, H. Zhang, M. Xiao, J. Ge, Z. Jiang, J. Wang, D. Tang, X. Cao, C. Liu, W. Xing, *Nat. Commun.* **2018**, *9*, 2120.

[29] C. Li, S. Yan, J. Fang, *Small* **2021**, *17*, 2102244.

[30] D. Iglesias, S. Ippolito, A. Ciesielski, P. Samorì, *Chem. Commun.* **2020**, *56*, 6878.

[31] D. Voiry, A. Mohite, M. Chhowalla, *Chem. Soc. Rev.* **2015**, *44*, 2702.

[32] J. Liu, J. P. Mater, J. Liu, J. Ma, Z. Zhang, Y. Qin, Y. Wang, Y. Wang, R. Tan, X. Duan, T. Z. Tian, C. H. Zhang, W. W. Xie, N. Li, L. Yu, C. Yang, Y. Zhao, H. Zia, F. Nosheen, G. Zheng, S. Gupta, X. Wu, Z. Wang, J. Qiu, G. Zhou, L. Xu, K. Liu, J. Fu, *J. Phys. Mater.* **2021**, *4*, 022004.

[33] P. D. Tran, T. V. Tran, S. Orio, S. Torelli, Q. D. Truong, K. Nayuki, Y. Sasaki, S. Y. Chiam, R. Yi, I. Honma, J. Barber, V. Artero, *Nat. Mater.* **2016**, *15*, 640.

[34] F. Fréchard, P. Sautet, *Surf. Sci.* **1995**, *336*, 149.

[35] G. Giuffredi, T. Asset, Y. Liu, P. Atanassov, F. Di Fonzo, *ACS Mater. Au* **2021**, *1*, 6.

[36] W. Zhao, Y. Li, W. Duan, F. Ding, *Nanoscale* **2015**, *7*, 13586.

[37] M. Chen, Y. Liu, Y. Zhang, G. Xing, Y. Tang, *Chem. Commun.* **2022**, *58*, 3591.

[38] A. J. Martinolich, J. J. Zak, D. N. Agyeman-Budu, S. S. Kim, N. H. Bashian, A. Irshad, S. R. Narayan, B. C. Melot, J. N. Weker, K. A. See, *Chem. Mater.* **2021**, *33*, 378.

[39] J. Xu, X. Li, W. Liu, Y. Sun, Z. Ju, T. Yao, C. Wang, H. Ju, J. Zhu, S. Wei, Y. Xie, *Angew. Chem., Int. Ed.* **2017**, *56*, 9121.

[40] T. A. Zepeda, N. L. Torres-García, J. Antúnez-García, D. H. Galván, B. Pawelec, R. Huirache-Acuña, J. N. D. de León, G. Alonso-Núñez, J. L. G. Fierro, S. Fuentes, *Appl Catal B* **2019**, *251*, 143.

[41] Q. Wan, X. Chen, Y. Gui, *ACS Omega* **2020**, *5*, 8919.

[42] G. Y. Gou, B. C. Pan, L. Shi, *Phys. Rev. B: Condens. Matter Mater. Phys.* **2007**, *76*, 155414.

[43] J. Dong, H. Hu, H. Li, G. Ouyang, *Phys. Chem. Chem. Phys.* **2021**, *23*, 20574.

[44] Y. Gu, Y. Katsura, T. Yoshino, H. Takagi, K. Taniguchi, *Sci. Rep.* **2015**, *5*, 12486.

[45] T. Zhang, Y. Liu, J. Yu, Q. Ye, L. Yang, Y. Li, H. J. Fan, *Adv. Mater.* **2022**, *34*, 2202195.

[46] A. Han, X. Zhou, X. Wang, S. Liu, Q. Xiong, Q. Zhang, L. Gu, Z. Zhuang, W. Zhang, F. Li, D. Wang, L. J. Li, Y. Li, *Nat. Commun.* **2021**, *12*, 709.

[47] H. Jin, T. Song, U. Paik, S. Z. Qiao, *Acc. Mater. Res.* **2021**, *2*, 559.

[48] M. Mattinen, M. Leskelä, M. Ritala, *Adv. Mater. Interfaces* **2021**, *8*, 2001677.